Journal of Nuclear Materials 543 (2021) 152581

Contents lists available at ScienceDirect

Journal of Nuclear Materials

journal homepage: www.elsevier.com/locate/jnucmat

Raman spectroscopy coupled to principal component analysis for studying UO_2 nuclear fuels with different grain sizes due to the chromia addition

A. Milena-Pérez [a], L.J. Bonales [a,b,*], N. Rodríguez-Villagra [a], S. Fernández [a], V.G. Baonza [c], J. Cobos [a,d]

[a] Centro de Investigaciones Energéticas, Medioambientales y Tecnológicas (CIEMAT). Avda. Complutense 40, 28040, Madrid, Spain
[b] Centro de Astrobiología (CSIC-INTA), Ctra. Ajalvir km. 4, 28850, Madrid, Spain
[c] MALTA-Consolider Team, Dep. Química Física, Fac. Ciencias Químicas, Universidad Complutense and Instituto de Geociencias IGEO (CSIC-UCM), 28040, Madrid, Spain
[d] Estación Biológica de Doñana (EBD-CSIC). Avda. Américo Vespucio 26, 41092, Sevilla, Spain

ARTICLE INFO

Article history:
Received 29 June 2020
Revised 5 September 2020
Accepted 4 October 2020
Available online 8 October 2020

Keywords:
Chromia-doped UO_2
Raman Spectroscopy
Principal Component Analysis
Grain size

ABSTRACT

Current necessities of nuclear power plants have led to increase burn-up of the fuel during operation. In this context, some undesirable processes, such as a higher release of gaseous fission products, may occur. New UO_2-based fuels are being developed by adding doping agents. Chromia (Cr_2O_3) has proved to considerably enhance grain growth during sintering, and thus promote the retention of these fission products. The study of these Cr-doped UO_2 fuels at *in situ* conditions would allow testing the real performance of the fuel in operating conditions. The existence of Raman portable instruments makes this scenario feasible. But first, the measurement protocols need to be developed. Therefore, in this paper, we explore the use of Raman spectroscopy as an approach for the analysis of the effect of Cr_2O_3 addition in a set of UO_2–Cr_2O_3 sintered pellets. The validity of Raman is demonstrated by using Principal Component Analysis (PCA). Three Principal Components describe 98.8% of the total variance of the data, and they are related to the main Raman modes of the samples. In addition, SEM images have shown the presence of bigger precipitates of Cr_2O_3 not only when the solubility limit of Cr^{3+} is exceeded, but also when it is not reached. By XRD, the well-known Vegard behavior is observed, and a solubility limit of Cr^{3+}dissolved into the UO_2 matrix is found to be (748±16) ppm for the particular sintering conditions used.

1. Introduction

Nowadays, current necessities of the nuclear facilities have led to increase the burn-up in operating reactors, with the aim of making the most of the fuel power in those UO_2-based fuels. In fact, current Light Water Reactors (LWR) are typically designed to achieve a burn-up about 50 GWd/tU, but with newer fuel technology (*i.e.* doped fuels), these same LWRs are now capable of achieving up to 60 or even 70 GWd/tU with the present enrichment limit (between 3 and 5% ^{235}U) [1–3]. However, several processes need to be taken into consideration at high burn-up. Especially important are the fission gas release and the pellet-cladding interaction, which decreases the flexibility of the reactor, *i.e.*, reduces the capability of the reactor to extend the burn-up in the established security requirements [4]. Both processes could compromise the safety margins in nuclear power plants, and needs to be minimized.

In view of the events that occurred at the Fukushima Daiichi nuclear power plant in March 2011, one of the most accepted concepts to this problem is the use of improved fuels referred as Accident-Tolerant Fuel (ATF) [5], made by the refinement of the fuel microstructure by using different dopants and clad designs. The purpose of these additives is to increase the fuel resistance by means of an enlargement of the average grain size of the matrix (densification) and the plasticity of the fuel. It is known that this change in grain size alters the diffusion phenomena inside the fuel pellets, causing an increased retention of the gaseous products inside the ceramic [6].

In order to address this issue, different dopants have been considered through the years, including oxides of chromium [4,7–10], magnesium [8,11], niobium [12–14] or titanium [15,16], among others. In addition, several investigations have been carried out

* Corresponding author at: Department of Molecular Evolution, Centro de Astrobiología (CAB-CSIC), Instituto Nacional de Técnica Aeroespacial (INTA), Carretera de Ajalvir km. 4, 28850 Torrejón de Ardoz, Madrid, Spain.
E-mail address: ljbonales@cab.inta-csic.es (L.J. Bonales).

https://doi.org/10.1016/j.jnucmat.2020.152581
0022-3115/

studying the performance of some of these dopants together, *e.g.* aluminosilicates [17]. Among them, chromia (Cr_2O_3) doped fuel has turned out to be an especially effective alternative to traditional UO_2 fuel (today used in LWRs) in the grain growth process during sintering, also showing a great improvement on pellet-cladding interaction and fission gas retention [4,10,18,19]. In fact, adding an amount of chromia close to the solubility limit has demonstrated to improve this behavior [10].

A wide variety of characterization techniques has been set to study chromia doped fuels [4,6,7,10]. Among them, X-Ray Diffraction (XRD) is the most frequently applied to deduce if the fluorite-type cubic structure is maintained with the increasing Cr_2O_3 concentration [4]. Scanning Electron Microscopy (SEM) has also been widely used in Cr_2O_3 doped fuels, mainly to confirm the increased grain size of the Cr-doped samples as a consequence of the chromium effect [7]. Some other techniques, such as X-Ray Photoelectron Spectrometry (XPS), Electron Microprobe Analysis (EPMA) and Differential Scanning Calorimetry (DSC) have been also used in order to characterize Cr-doped fuels [1,10,20].

On the other hand, as far as our knowledge, previous studies are lacking in the literature about the use of Raman spectroscopy to characterize Cr_2O_3-doped UO_2, in spite of have been widely used in the characterization of spent nuclear fuels analogues, such as UO_2 doped with different fission products, including gadolinium [20–22], neodymium [23,24], lanthanum [25], cerium [26], or SIMFUEL (SIMulated high burn-up FUEL, a spent nuclear fuel surrogate based on UO_2 doped with fission products) [20,27]. This technique meets two relevant features: it allows focusing on a specific area of few micrometers size of the sample, and it provides a spectral fingerprint to distinguish between chemically similar compounds. However, the main advantage of this technique is the possibility to perform *in-situ* measurements with the aim to track different processes that may occur to the samples, such as oxidation, thermal decomposition, hydrolysis reactions, etc., in controlled conditions of temperature and gaseous atmosphere. This property allows studying different materials in their original conditions, due to the existence of portable Raman instruments which could accomplish these *in-situ* measurements; *i.e.* real Cr-doped fuel could be studied and its performance could be tested. Thus, in this work we take advantage of Raman spectroscopy combined with multivariate analyses. The advent of spectroscopy techniques coupled with multivariate analysis, such as Principal Components Analysis (PCA) is being increasingly used in more and different fundamental and applied fields [28–32]. Nowadays, the multivariate analysis is not only performed by sophisticated tools. In fact, due to the development of commercial statistical software, it is possible to perform a PCA in an easy and fast way [33].

In order to achieve these goals, measurements protocols need to be developed and optimized, so they can be applied at *in-situ* conditions. Therefore, in this paper our work of Raman spectroscopy combined with PCA is completely new in the field of the solid dissolution of Cr_2O_3 into the UO_2 matrix. This work is part of a broader investigation of doped fuels within the frame of the European DisCo project (EC H2020 program, grant agreement 755,443), where once a complete Raman analysis is performed for this material, *in-situ* reactions will be studied to understand the behavior of the dopant and the improvement on the fuel properties.

In this work, a series of solid-solutions of UO_2 and $U_{1-y}Cr_yO_{2-x}$ pellets, prepared in order to cover all possible scenarios concerning the solubility of Cr_2O_3 in the UO_2 matrix [4,10], including both the solid solution of Cr_2O_3 in the matrix (solubility limit not reached) and the presence of chromia precipitates (beyond the solubility limit). These samples were analysed and characterised by SEM and XRD. Then, Raman spectroscopy as an analytical technique, and PCA as a multivariate analysis method were used to evaluate whether Raman spectroscopy could be employed to discern between fuels with different grain sizes due to the addition of chromia. Once we have demonstrated that it is possible to make use of this spectroscopy technique, a detailed evaluation of the Raman spectra is performed.

Thereby, the work is structured as follows: in Section 2, the fabrication method used to obtain the samples and the characterization techniques used are described. In addition, the characterization of raw materials is presented. In Section 3, SEM images are used to evaluate the effect of chromium in the UO_2 fuel in terms of the increase in grain size, and XRD results are discussed. Also in this section, PCA results show the applicability of Raman as a tool to characterize Cr-doped fuel, and Raman spectra are presented and described in detail. Finally, the conclusions of this work are presented in Section 4.

Table 1
Raw material characterization.

Material	SSA (BET) ($m^2\ g^{-1}$)	Average particle size (μm)
UO_2	0.95±0.02	15.23±0.57
Cr_2O_3	3.47±0.02	2.09±0.34

2. Materials and methods

2.1. Sample preparation

UO_2 and Cr_2O_3 powders were provided by ENUSA and Alfa Aesar, respectively. UO_2 was thermally annealed in a 4.7% H_2–N_2 atmosphere at 1100 °C to attain stoichiometric $UO_{2.00}$. UO_2 was mixed with weighted amounts of Cr_2O_3, together with $1^w/_o$ of EBS (Ethyl Bis Stearamide, $C_{38}H_{76}N_2O_2$, supplied by Tokyo Chemical Industry) as binder and lubricant [34], using low-energy ball milling. These batches of mixed powders were then blended for 1 min at 15 Hz in the mixer mill. Then, following a conventional metallurgical procedure, the mixtures obtained were subjected to uniaxial pressing with an applied pressure of 700 MPa in a press of 25 tons C256C (Power team, Johannesburg, South Africa). After that, a heating process under a 4.7% H_2–N_2 flow –in order to avoid UO_2 oxidation– was conducted on all the green pellets. All disks were then calcined in three stages (100, 300 and 500 °C) at 10 °C min^{-1} and held up to 4 h to remove the incorporated EBS, followed by the sintering process at 1675ºC for 4 h (5 °C min^{-1}). Finally, polishing and thermal annealing were carried out to reveal grains (10 min at 1590 °C under a 4.7% H_2–N_2 atmosphere). This fabrication process has been previously tested in our laboratory [35]. As a result, a series of Cr_2O_3-doped UO_2 solid solutions were obtained. An undoped UO_2 sample was also prepared following the same procedure. Prior to the sintering of the samples, raw powders have been characterized in terms of the Specific Surface Area (SSA) by BET with N_2 (ASAP 2020 Micromeritics) and the mean particle size by Laser Diffraction (Malvern, Series 2600). The results of this characterization can be seen in Table 1.[1]

In addition, starting powders have also been measured by Raman spectroscopy and observed by SEM. Raman spectrum of UO_2 powder (Fig. 1 at top) shows the well-known features of uranium dioxide: a) the triply degenerate T_{2g} mode at 445 cm^{-1}, b) the almost indistinguishable LO mode at about 570 cm^{-1}, and c) the first overtone of the LO mode (2LO) centered about 1140 cm^{-1} [36–38]. These bands are summarized in Table 2 (a-c). In addition,

[1] It is important to highlight that the average particle size presented in Table 1 refers to the average diameter of a discrete solid material, in this case a powder, and it is not related with the grain size, which refers to the average diameter of the individual crystal orientations located in poly-crystalline materials, and measured by SEM and presented further on for sintered pellets.

Table 2
Raman modes of starting powders used in this work.

Experimental Raman shifts for UO_2 (±1 cm^{-1})	Raman shifts for UO_2 (cm^{-1}) by other authors [37,38]	Raman mode assigned (UO_2) [37,38]
a) 445	445 [37,38]	T_{2g} [37,38]
b) 570	575 [37]	LO phonon [38]
c) 1140	1150 [37,38]	2LO phonon overtone [37,38]
Experimental Raman shifts for Cr_2O_3 (±1 cm^{-1})	Raman shifts for Cr_2O_3 (cm^{-1}) by other authors [39,40,42]	Raman mode assigned (Cr_2O_3) [39,40,42]
d) 303	303 [42]	A_{1g} [42]
e) 344	348 [42]	E_g [42]
f) 390	397 [42]	E_g [42]
g) 524	530 [42]	E_g [42]
h) 543	547 [42]	A_{1g} [42]
i) 601	609 [42]	E_g [42]
j) 680	691 [39,40]	CrO_2 [39,40]

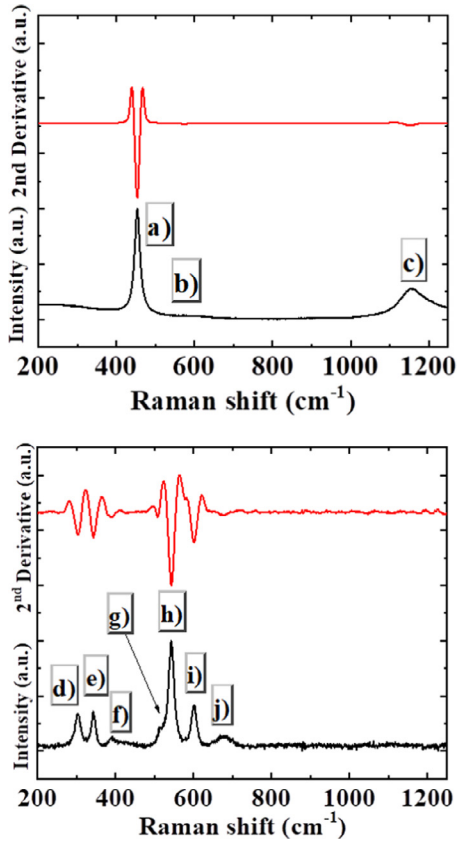

Fig. 1. Raman spectra of UO_2 (top) and Cr_2O_3 (bottom) and 2nd derivative curves. Labels a) to j) correspond to the Raman modes found in the spectra, assigned in Table 2.

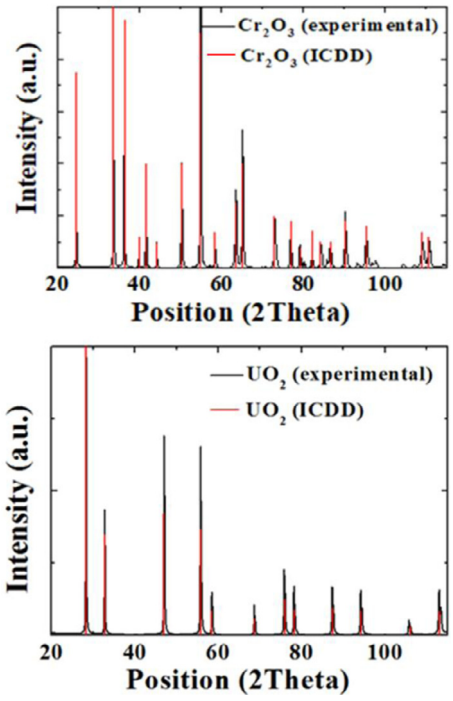

Fig. 2. XRD patterns of starting Cr_2O_3 (top) and UO_2 (bottom), together with their respective ICDD reference data.

Cr_2O_3 spectrum (Fig. 1 at bottom) shows the classic bands and features described in the literature [39–42]. The corresponding Raman shifts of both materials are shown in Table 2 (d-j), together with the Raman modes that represent. In both cases, spectra shown in Fig. 1 are the sum of 10 spectra of each powder.

Starting powders have been characterized, in terms of their XRD patterns, and compared with the standards, retrieved from ICDD references 03–065–0285 (UO_2) and 00–006–0504 (Cr_2O_3), in order to confirm the purity of the materials. The results can be seen in Fig. 2.

Finally, SEM images have been also acquired from each starting powder. A representative example of each one is shown in Fig. 3. In both cases, SEM observations reveal that the powder morphology consists of blunt and round particles, similar to microspheres. This shape is appropriated in the sintering of the pellets [43]. It is also remarkable the fact that particle size of Cr_2O_3 is smaller than UO_2, as presented in Table 1 and seen in Fig. 3.

2.1.1. SEM

Sample surface morphology has been visualized by means of a TM4000 Plus SEM by HITACHI, using a working voltage of 10 kV. The shape of the grains formed with different amounts of dopant was observed, as well as grain size of the samples was estimated by means of the linear intercept method [45]. The microscope is equipped with a Back-Scattering Electrons (BSE) detector, which provides clear images about pellets surfaces components, and a Secondary Electrons (SE) detector, which gives information about the relief of the surfaces. The combination of both has allowed us identifying different precipitates on the surface, which have been related to the segregation of Cr_2O_3 in the pellets.

2.1.2. XRD

XRD characterization was performed by means of a Bruker D8 Advance Eco diffractometer using Cu Kα radiation (λ=1.54056 Å) and operating at 40 kV and 25 mA. Bragg-Brentano configuration geometry was used. The 2θ range covered was from 20° to 120°, with 0.015° scanning steps and a primary slit of 0.5°. Diffracted ra-

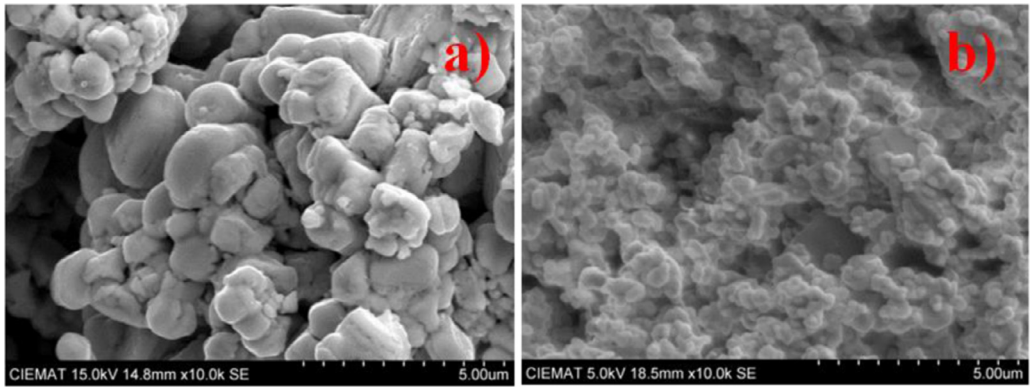

Fig. 3. SEM images of starting powders of a) UO_2 and b) Cr_2O_3.

diation was collected by a 1-dimensional Lynx Eye Position Sensitive Detector (PSD). The detector angular aperture was of 2.9°. Four to six XRD patterns were acquired under identical conditions for each sample. The uncertainty of each XRD measurement was estimated as the standard deviation of the individual measurements. Identification of each phase in the samples has been carried out by comparison with the ICDD data files. Finally, lattice parameter of each sample has been calculated by using the unit cell refinement process provided by the software TOPAS (Bruker Analytical X-Ray Systems), taking the $Fm\bar{3}m$ space group. All systematic sources of error, such as zero displacement, peak positions and goniometer shift, have been corrected by both a correct alignment of the instrument and measurement of a certified pattern of Al_2O_3.

2.1.3. Raman spectroscopy and PCA

Raman spectra were acquired by using a Horiba LabRam HR evolution spectrometer (Jobin Yvon Technology) using a He-Ne laser with wavelength equal to 632.8 nm. The laser beam was focused onto the sample through the 50x objective of an Olympus BX41 microscope. The sample is housed in the stage of the microscope without any previous treatment after the fabrication process and the polishing stage. A typical spectrum was obtained in the range 150–2500 cm^{-1} within 40 s of acquisition time. These acquisition conditions have been confirmed as low enough to not oxidize the surface of the pellets by local heating [44]. Acquired spectra were recalibrated by using the emission lines of a Ne arc-lamp. 10 spectra were acquired for each sample at different locations of the disks due to the heterogeneity of the pellets.

For the processing of the data, acquired spectra were subjected to multivariate analyses. Specifically, Principal Component Analysis (PCA) was carried out with the use of the OriginPro software (OriginLab, Northampton, MA, USA). Raman spectra were first baseline corrected using LabSpec 6.5 Spectroscopy suite (Horiba Scientific).

3. Results and discussion

In this work, a set of chromia-doped UO_2 disks have been sintered with different Cr_2O_3 concentrations. Table 3 shows the samples fabricated by this pathway.

In the next sections, the effect of chromia on the sintered pellets will be studied by using the aforementioned techniques.

3.1. SEM results

3.1.1. Grain size

As stated previously, doping UO_2 fuel with chromia has demonstrated to improve the performance of the fuel during irradiation in the reactor by increasing grain size, which allows a higher retention of fission products. In the analyzed samples, grain size has been measured by taking SEM images and then using the linear intercept method [46]. Representative images used for the calculation are shown in Fig. 4, where an increase in the grain size can be seen when increasing Cr_2O_3 concentration and compared to pure UO_2. Quantitative results of the average grain size in the doped pellets studied in this work are plotted in Fig. 5.

Table 3
Definition of samples.

Labeled Material	Cr_2O_3 added (ppm)
UO_2	0
UO_2_200Cr_2O_3	200
UO_2_600Cr_2O_3	600
UO_2_1000Cr_2O_3	1000
UO_2_6000Cr_2O_3	6000

The distribution of the results shown in Fig. 5 is analogous to grain size curves obtained in the same kind of fuels [7], but varying the absolute values, which depend on the specific sintering and annealing conditions (primarily heat treatment cycles: heating rates, holding time and temperature). Grains of undoped UO_2 (0 ppm of Cr_2O_3 added) have the same average grain size that the Cr-doped sample with the lowest amount of dopant (200 ppm). These similar values suggest that a significant concentration of dopant is needed to appreciate the effects on the grain growth. When increasing Cr_2O_3 concentration, grain sizes are higher, reaching a maximum when 1000 ppm of Cr_2O_3 are added. With even higher values of dopant, average grain size decreases (Fig. 5), thus demonstrating that the solubility limit has been reached and no more chromium enters into the UO_2 matrix. Beyond this solubility limit, excess dopant remains as inclusions in the grain boundaries, as proposed by Bourgeois et al. [7]. The presence of such precipitates inhibits the growth of the grains, *i.e.* the maximum grain size is obtained when the solubility limit of Cr^{3+} in UO_2 is reached (Fig. 6).

3.1.2. Segregated phases

For each sintered disk, SEM images have been taken covering the major part of the surfaces, looking for segregated phases on the pellet. More and bigger precipitates were observed in the samples with a higher Cr_2O_3 content, especially in the sample with the highest concentration, 6000 ppm. This fact is expected taking into account that, in samples doped with 6000 ppm Cr_2O_3, chromium is beyond the solubility limit in the UO_2 matrix. However, even though in the other samples the solubility limit has not been reached yet, several small precipitates are still observed. This could be a result of the slow incorporation kinetics of Cr into the

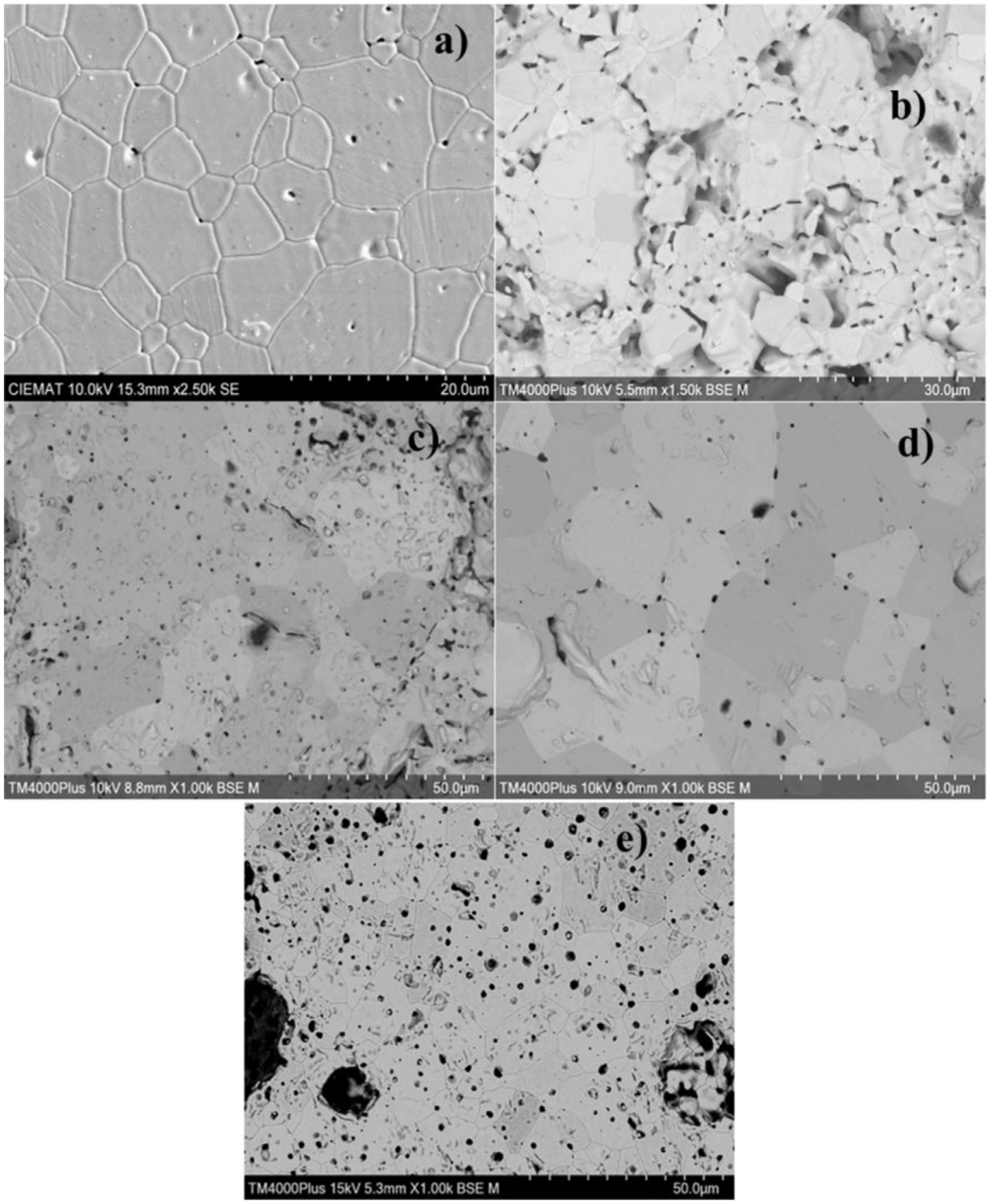

Fig. 4. Representative SEM images of the analyzed pellets: a) pure UO_2, b) UO_2_200Cr_2O_3, c) UO_2_600Cr_2O_3, d) UO_2_1000Cr_2O_3, e) UO_2_6000Cr_2O_3.

UO_2 matrix, and therefore the precipitates could be associated to the remnant of the initial powder particles, that are not dissolved [4].

Two images of representative Cr_2O_3 precipitates are shown in Fig. 6. As can be seen (Fig. 6a), the morphology of the precipitate, its size and the fact that it appears in the grain boundary could lead us to propose a chromium segregation, according to Yang et al. [47] and Bourgeois et al. [7]. Increasing the Cr_2O_3 concentration and exceeding the solubility limit, sample doped with 6000 ppm, the amount precipitated is much bigger, although it still appears in grain boundaries, as expected (Fig. 6b).

3.2. XRD

In order to study the lattice parameter evolution of the UO_2 pellets due to the presence of chromia, XRD was used and the corresponding diffractograms were obtained (Fig. 7). It is known that the crystal structure of UO_2 is cubic, fluorite-type, so the lattice is characterized by only one lattice parameter (a). Diffraction peaks of all prepared samples were acquired under the same conditions, and a value for the lattice parameters was obtained from each one by using the unit cell refinement method, applying the corresponding error corrections. They are plotted in Fig. 8.

From the diffraction peaks of each sample (Fig. 7a), it can be seen that there is a shift to higher 2θ values with increasing Cr_2O_3 concentration. This effect is clearly observed in the 113° doublet (Fig. 7b), indicating that the lattice parameter of the doped sample is smaller than that of undoped UO_2, and the higher the concentration of dopant is, the lower lattice parameter value. This fact supports the densification of the samples. This lattice contraction as a consequence of introduction of chromium into the cubic UO_2 lattice is consistent with XRD results from Cardinaels et al. [10].

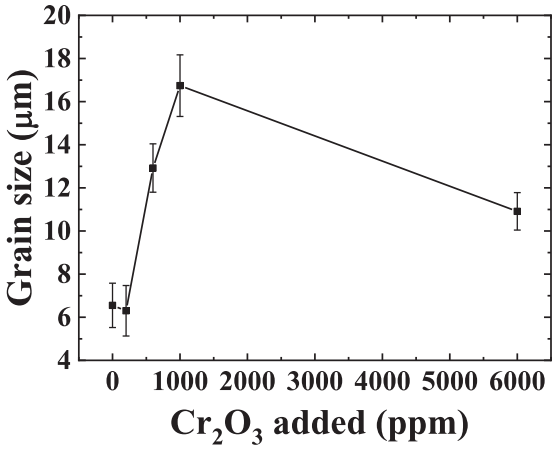

Fig. 5. Average grain size of the studied disks *vs* Cr_2O_3 content. Uncertainty bands correspond to the repeatability of the measurements.

To clearly visualize this lattice contraction as a function of chromium concentration, in Fig. 8 the lattice parameter of the fabricated pellets *versus* the chromium mixed with the UO_2 in the monoliths fabrication is plotted. It can be seen that lattice parameter decreases linearly as a function of the chromia concentration until the solubility limit is reached. Nevertheless, the sample doped with 6000 ppm of Cr_2O_3 does not follow the same trend, due to the dissolution of the Cr^{3+} into the matrix reached the solubility limit under the conditions used in the fabrication of the pellet in this work, which according to the sintering conditions was established around 1000 ppm of Cr_2O_3 [4,10].

In the selected range, the decrease in the lattice parameter follows a linear trend according to Eq. (1) in a good agreement with Vegard's law, which states that the lattice parameter of solid solutions vary linearly with the composition [48].

$$a(\text{nm}) = -1.92(\pm 0.25)\cdot 10^{-7}[Cr_2O_3](\text{ppm}) + 0.54724(\pm 0.00002) \quad (1)$$

The Vegardś law-like behavior when doping UO_2 with chromia has been also found by other authors [4,10]. The contraction of the cubic lattice of UO_2 can be explained taking into account the defects that are created with the incorporation of a Cr^{3+} ion. When a U^{4+} ion is substituted by a Cr^{3+} ion, defect clusters are formed in order to maintain electroneutrality within the structure [7,10]. The charge defect introduced in the lattice can be neutralized whether with the oxidation to U^{5+} by a nearby uranium atom, or by introducing oxygen vacancies. The net result of both effects is a contraction in the lattice parameter [10], specially taking into account that the ionic radius of Cr^{3+} is much smaller than that of U^{4+} (61 and 114 pm, respectively [49]). This has been confirmed by Cardinaels et al. [10], by using interatomic potentials calculations.

Although the Vegardś law-like behavior has been confirmed, it is valid only in the region where a complete solid solution is established [50]. This means that, from the data obtained by XRD, it is possible to deduce a solubility limit of Cr in the UO_2 matrix in these conditions. Assuming that beyond the solubility limit the lattice parameter will not further decrease, from the intersection of the Vegardś line and the horizontal line starting at the point of 6000 ppm of Cr_2O_3, this limit can be deduced; this calculation is rendered in Fig. 8 (red square). This method has been validated to estimate solubility limits in other systems, such as Nb-doped UO_2 [51]. For the precise mathematical calculation, it has been obtained a solubility limit of (1094 ± 23) ppm of Cr_2O_3, which corresponds to (748 ± 16) ppm of Cr^{3+}. This value is in good agreement with other studies carried out under similar sintering conditions, as reported by Leenaers et al. (860 ± 30 ppm of Cr^{3+} [4]) and Bourgeois et al. (750 ppm of Cr^{3+} [7]). In addition, this limit supports the grain size behavior described in the previous section, as the highest grain size is found in the sample closest to the solubility limit.

Fig. 9 shows a comparison between calculated lattice parameters and the grain size measurements of the chromia-doped UO_2 pellets. It should be highlighted that the maximum grain size is not reached with the lowest lattice parameter value. This is an indicator of the grain growth inhibition by the formation of precipitates in grain boundaries [7], a process that not always occur when solubility limit has been reached (for example due to the slow incorporation kinetics of chromium [4]). In fact, this lattice parameter is reached when doping with a Cr_2O_3 concentration far beyond the solubility limit (6000 ppm), but in this case, the presence of chromia in grain boundary is so high that the average grain size is even lower than pellets doped with 600 ppm of Cr_2O_3. The same reason of low incorporation kinetics of Cr^{3+} could also explain the behavior of the point labeled as UO_2_200Cr_2O_3 in Fig. 9, which does not follow the linear trend of the grain size values, indicating that a minimum chromium amount may be necessary to promote the enlargement of pellet grains.

3.3. Raman spectroscopy. principal component analysis (PCA)

Fig. 10 shows Raman spectra acquired from the UO_2 and chromia-doped UO_2 pellets. The plot represents the averaged spectra from 10 individual spectrums recorded at different locations of each disk.

The known Raman features of an undistorted, face-centered cubic structure like undoped UO_2 [44,52] are seen at Fig. 10. The same assignment that the one shown with powders (Table 2 entries a-c) is used here: T_{2g} mode at 445 cm^{-1}, the LO phonon at 570 cm^{-1} and the first overtone (2LO) at 1140 cm^{-1}. In addition, in some of the Raman spectra acquired from the doped pellets of this study, an extra feature to the previously described has been found. It is an intense doublet at around 1380 cm^{-1} and 1410 cm^{-1} (Fig. 10) that has been associated with fluorescence of Cr_2O_3 by several authors [41,53–55]. All these features have been individually analyzed in Section 3.4.

Because of the complexity of Raman spectra, a multivariate data analysis, via Principal Component Analysis (PCA), has been used in order to explore similarities and differentiate between samples of UO_2 fuels doped with different amounts of Cr_2O_3, which have led to different grain size pellets (Fig. 4). Thus, after grouping the spectra by the added amount of Cr_2O_3 into five data set (0, 200, 600, 1000, and 6000 ppm) a PCA has been performed. This analysis reduces the initial spectra data to a number of variables of principal components (PC) [33]. In technical terms, PC approach would neatly simplify the interpretation of our compiled variables by finding patterns in the information provided by the Raman spectral data.

From this analysis, the first result is to calculate in how many PC data can be grouped. This is given by the eigenvalue plot, shown in Fig. 11, and indicating that the greatest impact on the variance of the analyzed spectra registered for the five groups previously described can be related to the first three principal components [30]. Actually, the principal components PC1, PC2 and PC3 jointly explain 98.8% of the total variance of the data. PC1, PC2 and PC3 account for 89.8%, 7.7% and 1.3%, respectively.

Fig. 12 shows a three-dimension score plot of the relation of the three main PCs involved. An in-depth examination of the score plot of these three PCs reveals a clear distinction between the five groups of data regarding the five different amounts of Cr_2O_3 defined before. This indicates that the PCA performed led to a very good discrimination between groups of samples.

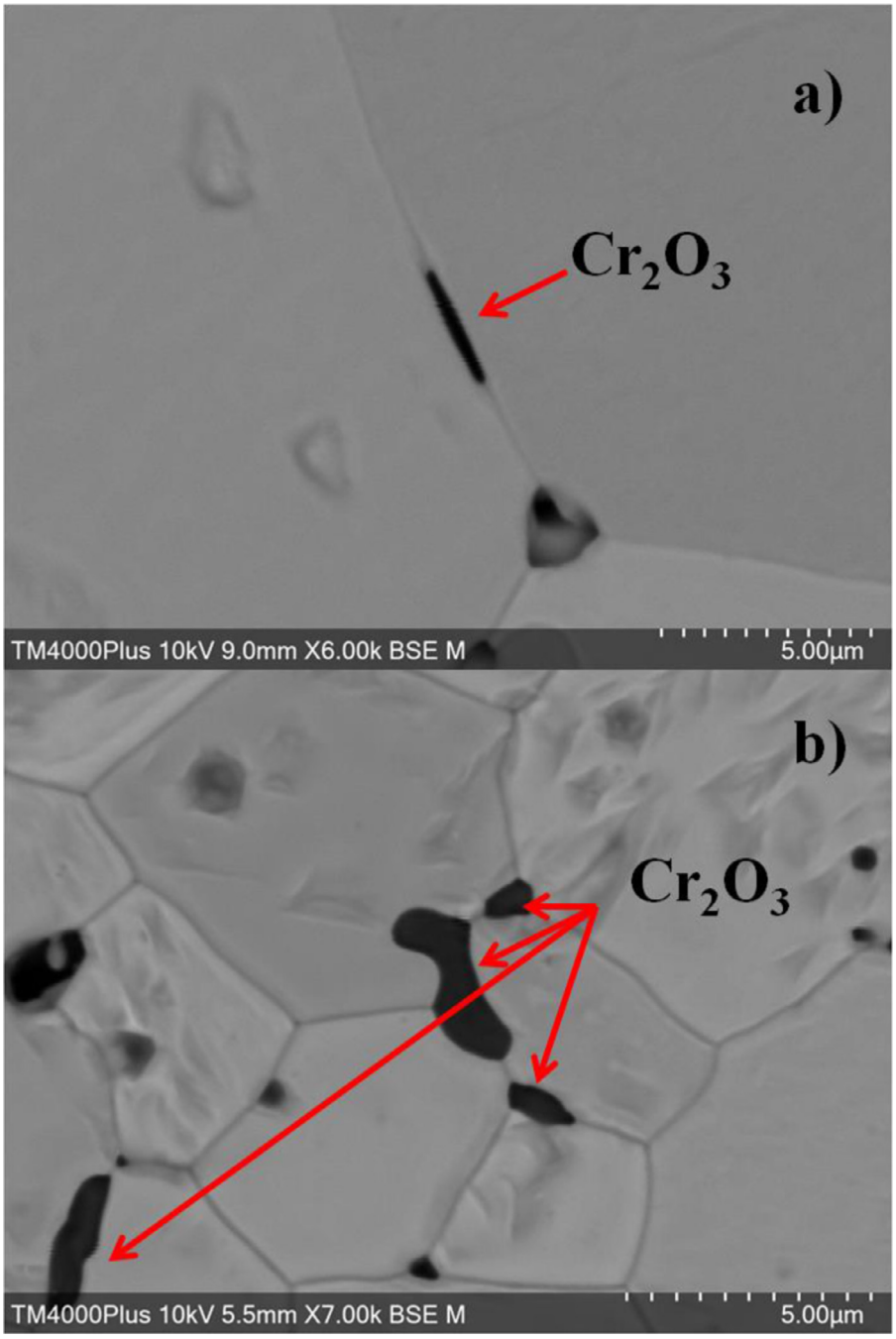

Fig. 6. Back scattered SEM images of chromium precipitates in a grain boundaries in samples doped with a) 1000 ppm and b) 6000 ppm of Cr_2O_3, respectively. (For interpretation of the references to colour in this figure legend, the reader is referred to the web version of this article.)

3.4. Raman and fluorescence spectral analysis

3.4.1. Fluorescence

The presence of the formerly described fluorescence peaks is a consequence of a Cr_2O_3-enriched region where the Raman laser spot has acquired the spectrum, thus there is chromium present at the surface of the pellet and has not entered in the UO_2 matrix. This hypothesis suggests that the higher Cr_2O_3 precipitates in the pellet-surface, the higher probability of finding fluorescence peaks in the Raman spectra, which are acquired 10 times per pellet randomly along the surface. Despite this reduced statistical sampling, the frequency histogram shown in Fig. 13 confirms this hypothesis. This finding supports the behavior of Cr_2O_3 previously revealed in the SEM section, as more peaks assigned to the fluorescence of Cr^{3+} are found in the sample that presents more Cr_2O_3 precipitates, *i.e.* UO_2_6000Cr_2O_3.

3.4.2. Raman intensity

On the one hand, T_{2g} and 2LO modes have been analyzed in terms of their intensities. The T_{2g} mode involves the U-O bond stretching, and 2LO is attributed to a crystal electric field transition. This latter band has been proposed as a fingerprint for a quasi-perfect fluorite lattice [22,56].

The observed intensity of the Raman scattered radiation depends, among other factors, on the instrumental and configuration parameters such as laser power or wavelength, optical path variations, sample placement acquisition and accumulation time, etc.

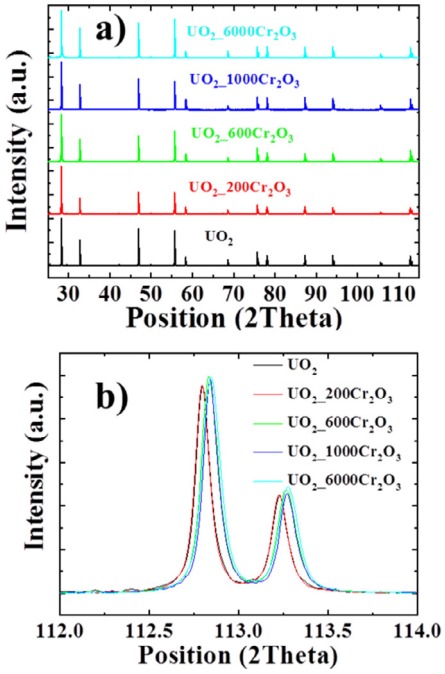

Fig. 7. a) Diffraction patterns of the studied samples and b) the (531) $K\alpha_{1,2}$ doublet at 113º of the normalized diffraction patterns.

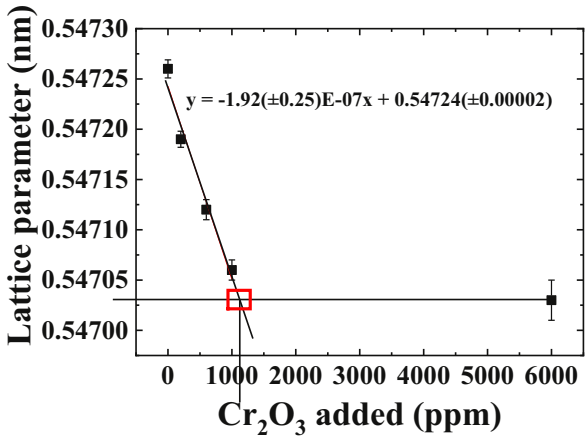

Fig. 8. Lattice parameter *vs* Cr_2O_3 concentration and graphical calculation of solubility limit of Cr_2O_3 in the UO_2 matrix for the samples studied. Uncertainty bands correspond to the repeatability of the measurements.

Here all these instrumental parameters have been kept constant to perform a comparison of the absolute intensity, which is related to the Raman cross-section. Fig. 14 shows the changes in absolute areas, *i.e.* integrated intensity, of the two mentioned bands. A marked decrease is observed when increasing Cr_2O_3 concentration, due to the distortions introduced in the lattice as a result of the entry of the doping agent. The fact that this area decrease is found in both peaks (445 and 1140 cm^{-1}) may indicate the unlikelihood that they can be attributed to variations in surface roughness.

3.4.3. Profile analysis of the LO band

On the other hand, the band at 570 cm^{-1} was analyzed in detail. A profile analysis was performed by obtaining the second derivative of the spectra. This analysis revealed the contribution of two Lorentzian peaks, which indicates the presence of an additional feature band centered at 545 cm^{-1} that was not observed in pure UO_2 spectra. This new feature and a more detailed study can be observed in Fig. 15.

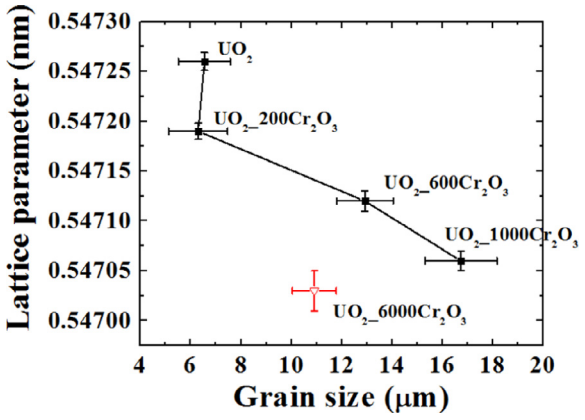

Fig. 9. Lattice parameter *vs* average grain size of the analyzed pellets. Black squares correspond to samples with Cr_2O_3 content lower than the solubility limit, while the open triangle represents the pellet doped with 6000 ppm of Cr_2O_3, which is higher than the solubility limit. Uncertainty bands correspond to the repeatability of the measurements.

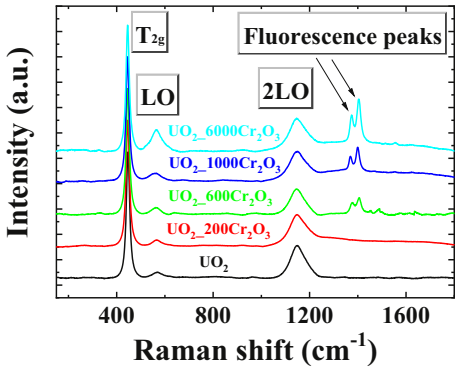

Fig. 10. Raman spectra of chromia-doped UO_2 pellets. .

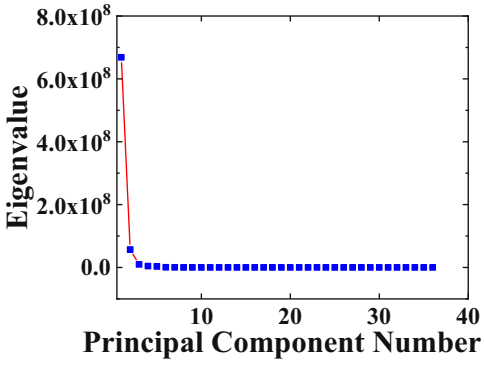

Fig. 11. Plot of eigenvalues for PCA of Raman spectra.

In Fig. 15, the LO mode at 570 cm^{-1} increases in intensity with chromia content, together with the band at 545 cm^{-1}. This latter band is not observed for pure UO_2, and it has been related to the creation of oxygen vacancies in other trivalent-doped UO_2 fuels systems, such as Gd and Dy [20], Nd [24], or La [25]; thus same assignment can be made when doping with Cr^{3+}. This is a result of the charge imbalance produced by the introduction of the trivalent dopant (substitution of a U^{4+} for a Cr^{3+}), and therefore produces a lattice distortion, as confirmed by XRD (see Section 3.2). In addition, the assignment of this feature to the presence of oxygen vacancies can be confirmed by comparing with the Raman spectroscopic studies performed by Rao et al. [57] with ThO_2-UO_2 solid solutions, who did not report the presence of this band from

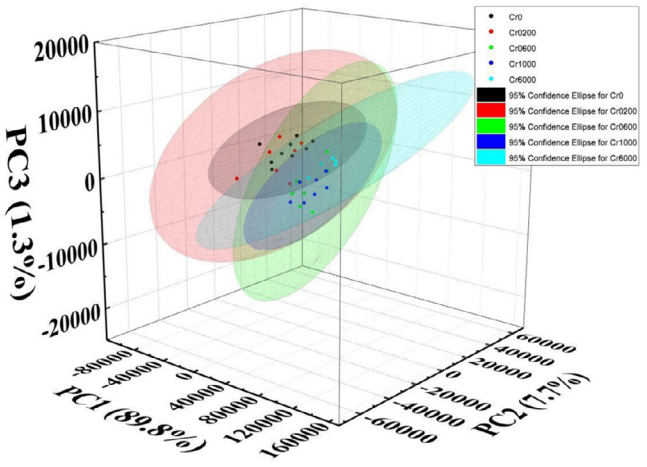

Fig. 12. 3D Score plot of Principal Components and their corresponding confidence (95%) ellipse based on different Cr_2O_3 contents in UO_2 pellets. The total percent variance captured by each PC is shown in brackets along each axis. (For interpretation of the references to colour in this figure legend, the reader is referred to the web version of this article.)

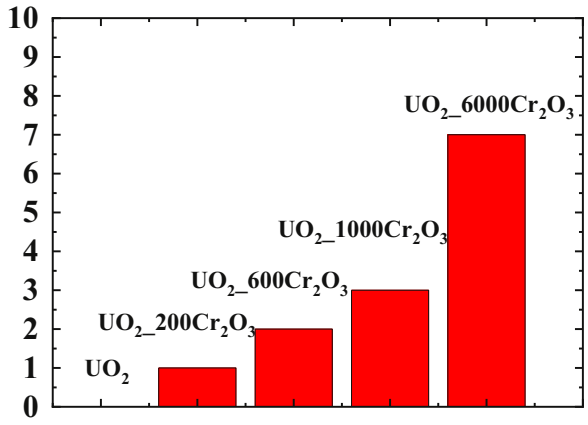

Fig. 13. Number of spectrums showing Cr^{3+}-fluorescence peaks (per 10 spectrums acquired for each simple). (For interpretation of the references to colour in this figure legend, the reader is referred to the web version of this article.)

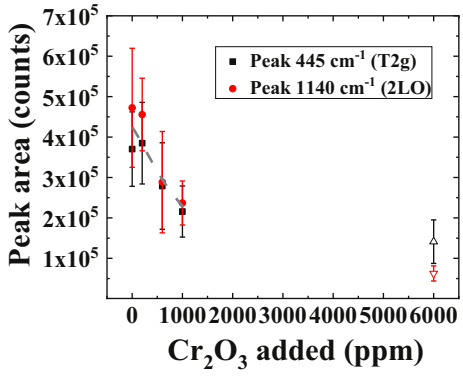

Fig. 14. Area evolution of the T_{2g} (445 cm^{-1}) and 2LO (1140 cm^{-1}) bands with Cr_2O_3 concentration. Solid symbols correspond to samples with Cr_2O_3 content lower than the solubility limit, while open triangles represent the pellet doped with 6000 ppm of Cr_2O_3, which is higher than the solubility limit. Dashed line represents a guide to the eye to show the general trend of data. Uncertainty bands correspond to the repeatability of the measurements.

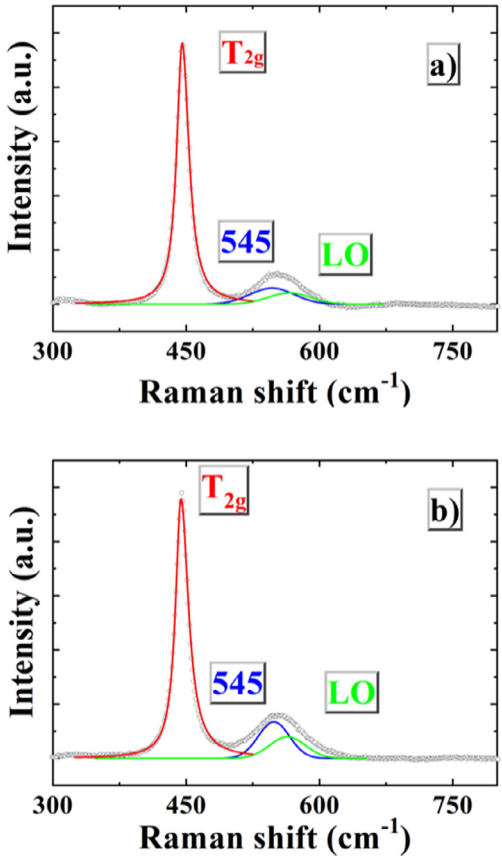

Fig. 15. Raman spectra of a UO_2 disk doped with a) 600 ppm and b) 1000 ppm of Cr_2O_3 by Lorentzian peaks at 445, 545 and 570 cm^{-1}.

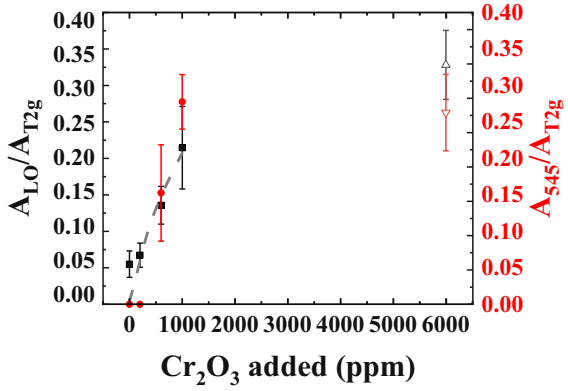

Fig. 16. Evolution of the intensity of the peaks at 570 cm^{-1} (LO band, black squares) and 545 cm^{-1} (red circles), both referred to the T_{2g} band, with the Cr_2O_3 content. Solid symbols correspond to samples with Cr_2O_3 content lower than the solubility limit, while open triangles represent the pellet doped with 6000 ppm of Cr_2O_3, which is higher than the solubility limit. Dashed line represents a guide to the eye to show the general trend of data. Uncertainty bands correspond to the repeatability of the measurements. (For interpretation of the references to colour in this figure legend, the reader is referred to the web version of this article.)

the analysis of Th^{4+} doped UO_2. In fact, the substitution of U^{4+} by Th^{4+} does not produce a charge imbalance and therefore no oxygen vacancies are created. It is important to highlight that this new band centered around 545 cm^{-1} has been observed only when Cr_2O_3 nominal concentration was beyond 600 ppm (Fig. 16).

The band at 570 cm^{-1} has been ascribed to a first-order LO phonon [36]. Its observation has been related to lattice distortions, causing a breakdown in the selection rules [37], and allowing the

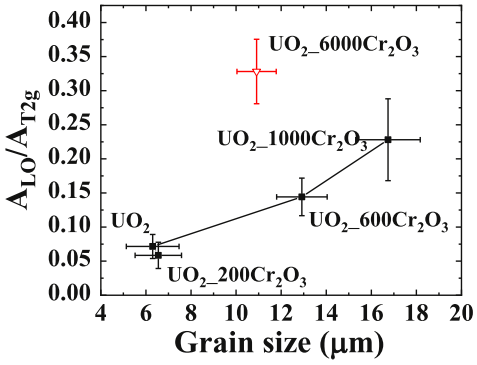

Fig. 17. LO band area ratio *vs* grain size of the analyzed pellets. Black squares correspond to samples with Cr_2O_3 content lower than the solubility limit, while the open triangle represents the pellet doped with 6000 ppm of Cr_2O_3, which is higher than the solubility limit. Uncertainty bands correspond to the repeatability of the measurements.

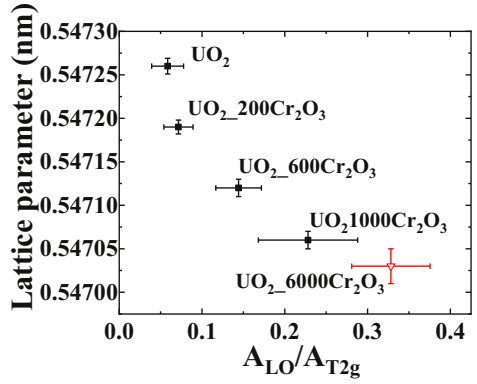

Fig. 18. Lattice parameter *vs* A_{LO}/A_{T2g} peaks ratio. Black squares correspond to samples with Cr_2O_3 content lower than the solubility limit, while the open triangle represents the pellet doped with 6000 ppm of Cr_2O_3, which is higher than the solubility limit. Uncertainty bands correspond to the repeatability of the measurements.

appearance of this forbidden Raman scattering mode. As in the previous case, similar bands have been observed in other systems, such as hyperstoichiometric UO_{2+x} [37] and for another kind of doped UO_2 materials [24,25].

The calculated area of these features and the area ratio relative to that of the T_{2g} band have been plotted against the Cr_2O_3 concentration added at the beginning of the sintering process. This plot can be seen in Fig. 16. This calculated ratio emphasizes the dependence of the oxygen vacancies in the matrix structure with increasing chromia content.

When detected, both the 545 and 570 cm^{-1} area ratios are in the same range, and both undergo the same increase with dopant concentration. These evidences strongly support the assumption that both features are related to the dissolution of Cr^{3+} in the UO_2 solid matrix and then, to defects in the fluorite lattice induced by oxygen vacancies.

Some authors have reported an additional band at 620–630 cm^{-1} associated with the presence of cuboctahedral clusters of the oxidized phase U_4O_9, both in UO_2 and rare-earth doped samples [21,23,58]. The lack of this band in our spectra testifies that this phase has not been formed on the surfaces of the samples studied in this work, due to the final preparation performed to the pellets during the sintering process (thermal treatment under reducing atmosphere; 4.7% H_2–N_2). In addition, it also confirms that no self-oxidation of the sample by laser heating during the measurements has occurred.

As done before for the XRD results (Fig. 9), the area ratio of this band has been compared with the average grain size values of the samples obtained by SEM (Fig. 17). Again, maximum grain size is not reached with maximum A_{LO}/A_{T2g}, due to the segregation in the grain boundaries of the Cr_2O_3 that has not been incorporated in the UO_2 matrix [4,7]. It should be highlighted that uncertainty intervals for samples UO_2 and UO_2_200Cr_2O_3 overlap, supporting that a minimum amount of Cr may be needed to promote grain enlargement.

Finally, from the combination of both XRD and Raman spectroscopy, one can extract interesting data that may help to understand the dissolution of Cr^{3+} into the UO_2 matrix. In Fig. 18, a plot of the lattice parameter obtained by XRD *versus* the area ratio of the LO band (570 cm^{-1}) relative to the T_{2g} mode (445 cm^{-1}) obtained by Raman is presented. The tendency shown by the points indicates stabilization around values close to the calculated solubility limit, approximately near the labeled point UO_2_1000Cr_2O_3, as the decrease in lattice parameter values and the increase in the area ratio are not so marked. The quasi-linear behavior between the lattice parameter and the area ratio is a further key indicator of the validity of Raman spectroscopy to analyze Cr-doped UO_2 pellets, since the correspondence with a well-established technique such as XRD is almost total.

4. Conclusions

Raman spectroscopy has been used to characterize Cr-doped UO_2 pellets for the first time. Its validity to study these samples has been demonstrated by means of the Principal Component Analysis (PCA) and a detailed interpretation of the spectral features. From the statistical analysis, it is found that 98.8% of the total variance of the data is explained by three Principal Components (PC). These PCs coincide with the main Raman features found for the sintered disks. The variation of the Raman modes with Cr_2O_3 concentration is studied and related to the creation of oxygen vacancies due to the entry of Cr^{3+} in the UO_2 matrix.

The study of the grain size of the doped samples reveals that the highest value is found for the sample with the amount of Cr_2O_3 closest to the solubility limit. This is interpreted in terms of the restriction of the grain growth by the presence of segregated phases. SEM images have shown that precipitates of Cr_2O_3 are found to be in the grain boundaries, and that more and bigger precipitates are found for the sample UO_2_6000Cr_2O_3. However, Cr_2O_3-rich areas in the surface of the pellets are also found in samples where the solubility limit has not been reached, probably due to the low incorporation kinetics of Cr. Its presence is supported by the appearance of their characteristic fluorescence peaks in several Raman spectra. Therefore, the quantity of doping agent and/or fabrication methods for real fuel must be optimized. By XRD, the solubility limit of Cr in these specific sintering conditions is estimated to be (748 ± 16) ppm.

In summary, a systematic measurement protocol by Raman spectroscopy has been successfully developed to characterize Cr-doped UO_2 fuels. Further work on how to implement these protocols to perform *in-situ* measurements on real fuel will be carried out, so realistic tests will be applicable to these new nuclear materials.

Data availability

The raw/processed data required to reproduce these findings cannot be shared at this time due to technical or time limitations.

Declaration of Competing Interest

The authors declare that they have no known competing financial interests or personal relationships that could have appeared to influence the work reported in this paper.

Acknowledgements

This work was supported by the Spanish MINECO projects ESP2017-89053-C2-1-P and PID2019-107442RB-C32, and the AEI project MDM-2017-0737 Unidad de Excelencia "María de Maeztu". Authors also want to thank the funding for this research from the European Commission Horizon 2020 Research and Training Programme DisCo (Modern Spent Fuel Dissolution and Chemistry in Failed Container Conditions), under grant agreement number 755443.

References

[1] J. Arborelius, K. Backman, L. Hallstadius, M. Limback, J. Nilsson, B. Rebensdorff, G. Zhou, K. Kitano, R. Lofstrom, G. Ronnberg, Advanced Doped UO_2 Pellets in LWR Applications, J. Nucl. Sci. Technol. 43 (2006) 967–976.
[2] Z. Guo, R. Ngayam-Happy, M. Krack, A. Pautz, Atomic-scale effects of chromium-doping on defect behaviour in uranium dioxide fuel, J. Nucl. Mater. 488 (2017) 160–172.
[3] K. Backman, L. Hallstadius, G. Roennberg, Westinghouse Advanced Doped Pellet-Characteristics and Irradiation Behaviour, IAEA-TECDOC-1654, International Atomic Energy Agency (IAEA), 2010.
[4] A. Leenaers, L. de Tollenaere, C. Delafoy, S. Van den Berghe, On the solubility of chromium sesquioxide in uranium dioxide fuel, J. Nucl. Mater. 317 (2003) 62–68.
[5] K.A. Gamble, G. Pastore, D. Andersson, and M. Cooper, "ATF material model development and validation for priority fuel concepts," United States, 2019.
[6] C. Riglet-Martial, P. Martin, D. Testemale, C. Sabathier-Devals, G. Carlot, P. Matheron, X. Iltis, U. Pasquet, C. Valot, C. Delafoy, R. Largenton, Thermodynamics of chromium in UO_2 fuel: a solubility model, J. Nucl. Mater. 447 (2014) 63–72.
[7] L. Bourgeois, P. Dehaudt, C. Lemaignan, A. Hammou, Factors governing microstructure development of Cr2O3-doped UO_2 during sintering, J. Nucl. Mater. 297 (2001) 313–326.
[8] S. Kashibe, K. Une, Effect of additives (Cr2O3, Al_2O_3, SiO_2, MgO) on diffusional release of 133Xe from UO_2 fuels, J/ Nucl. Mater. 254 (1998) 234–242.
[9] I. Greenquist, M. Tonks, M. Cooper, D. Andersson, Y. Zhang, Grand potential sintering simulations of doped UO_2 accident-tolerant fuel concepts, J. Nucl. Mater. 532 (2020) 152052.
[10] T. Cardinaels, K. Govers, B. Vos, S. Van den Berghe, M. Verwerft, L. de Tollenaere, G. Maier, C. Delafoy, Chromia doped UO_2 fuel: investigation of the lattice parameter, J. Nucl. Mater. 424 (2012) 252–260.
[11] T. Fujino, S. Nakama, N. Sato, K. Yamada, K. Fukuda, H. Serizawa, T. Shiratori, Solubility of magnesium in uranium dioxide, J. Nucl. Mater. 246 (1997) 150–157.
[12] H. Assmann, W. Dörr, G. Gradel, G. Maier, M. Peehs, Doping UO_2 with niobia — Beneficial or not? J. Nucl. Mater. 98 (1981) 216–220.
[13] J.C. Killeen, The effect of additives on the irradiation behaviour of UO_2, J. Nucl. Mater. 58 (1975) 39–46.
[14] S. Kun Woo, K. Si Hyoung, N. Sang Ho, L. Young Woo, Y. Myung Seung, Effects of Nb_2O_5 addition on grain growth and densification in UO_2 pellets under reducing and/or oxidizing atmospheres, J. Nucl. Mater. 209 (1994) 280–285.
[15] T. Yao, S.M. Scott, G. Xin, J. Lian, TiO_2 doped UO_2 fuels sintered by spark plasma sintering, J. Nucl. Mater. 469 (2016) 251–261.
[16] I. Amato, R.L. Colombo, A.P. Balzari, Grain growth in pure and titania-doped uranium dioxide, J. Nucl. Mater. 18 (1966) 252–260.
[17] K. Une, M. Hirai, K. Nogita, T. Hosokawa, Y. Suzawa, S. Shimizu, Y. Etoh, Rim structure formation and high burnup fuel behavior of large-grained UO_2 fuels, J. Nucl. Mater. 278 (2000) 54–63.
[18] A.R. Massih, Effects of Additives On Uranium Dioxide Fuel Behaviour, Swedish Radiation Safety Authority, 2014.
[19] J. Holm, Cr_2O_3 Doped UO_2 fuel, BWR Implementation, AREVA, Rockville, United States, 2015.
[20] M. Razdan, D.W. Shoesmith, Influence of Trivalent-Dopants on the Structural and Electrochemical Properties of Uranium Dioxide (UO_2), J. Electrochem. Soc. 161 (2013) 105–113.
[21] J. Lee, J. Kim, Y.-.S. Youn, N. Liu, J.-.G. Kim, Y.-.K. Ha, D.W. Shoesmith, J.-.Y. Kim, Raman study on structure of U1−yGdyO2−x (y=0.005, 0.01, 0.03, 0.05 and 0.1) solid solutions, J. Nucl. Mater. 486 (2017) 216–221.
[22] N. Liu, J. Kim, J. Lee, Y.-.S. Youn, J.-.G. Kim, J.-.Y. Kim, J.J. Noel, D.W. Shoesmith, Influence of Gd Doping on the Structure and Electrochemical Behavior of UO_2, Electrochim. Acta 247 (2017) 496–504.
[23] J. Lee, J. Kim, Y.-.S. Youn, J.W. Kim, S. Lim, Surface characterization of (U, Nd)O_2: the influence of trivalent-dopant on structure of UO_2, Progress in Nuclear Science and Technology 5 (2018) 33–36.
[24] L. Desgranges, Y. Pontillon, P. Matheron, M. Marcet, P. Simon, G. Guimbretière, F. Porcher, Miscibility Gap in the U–Nd–O Phase Diagram: a New Approach of Nuclear Oxides in the Environment? Inorg. Chem. 51 (2012) 9147–9149.
[25] Z. Talip, T. Wiss, P.E. Raison, J. Paillier, D. Manara, J. Somers, R.J.M. Konings, Raman and X-ray Studies of Uranium–Lanthanum-Mixed Oxides Before and After Air Oxidation, J. Am. Ceram. Soc. 98 (2015) 2278–2285.
[26] J.M. Elorrieta, L.J. Bonales, S. Fernández, N. Rodríguez-Villagra, L. Gutiérrez-Nebot, V.G. Baonza, J. Cobos, Pre-and post-oxidation Raman analysis of (U, Ce)O_2 oxides, J. Nucl. Mater. 508 (2018) 116–122.
[27] N. Rauff-Nisthar, C. Boxall, I. Farnan, Z. Hiezl, W. Lee, C. Perkins, R.J. Wilbraham, Corrosion Behavior of AGR Simulated Fuels – Evolution of the Fuel Surface, ECS Trans. 53 (2013) 95–104.
[28] V. Vujanovic, S.H. Kim, R. Lahlali, C. Karunakaran, Spectroscopy and SEM imaging reveal endosymbiont-dependent components changes in germinating kernel through direct and indirect coleorhiza-fungus interactions under stress, Sci. Rep. 9 (2019) 1665.
[29] Z.A. Abdel-Salam, S.A.M. Abdel-Salam, I.I. Abdel-Mageed, M.A. Harith, Evaluation of proteins in sheep colostrum via laser-induced breakdown spectroscopy and multivariate analysis, J. Adv. Res. 15 (2019) 19–25.
[30] A. Matwijczuk, T. Oniszczuk, A. Matwijczuk, E. Chruściel, A. Kocira, A. Niemczynowicz, A. Wójtowicz, M. Combrzynski, D. Wiacek, Use of FTIR Spectroscopy and Chemometrics with Respect to Storage Conditions of Moldavian Dragonhead Oil, Sustainability 11 (2019) 6414.
[31] M.D. Peris-Díaz, B. Łydżba-Kopczyńska, E. Sentandreu, Raman spectroscopy coupled to chemometrics to discriminate provenance and geological age of amber, J. Raman Spectrosc. 49 (2018) 842–851.
[32] O.A. Maslova, G. Guimbretière, M.R. Ammar, L. Desgranges, C. Jégou, A. Canizarès, P. Simon, Raman imaging and principal component analysis-based data processing on uranium oxide ceramics, Mater. Charact. 129 (2017) 260–269.
[33] D. Granato, J.S. Santos, G.B. Escher, B.L. Ferreira, R.M. Maggio, Use of principal component analysis (PCA) and hierarchical cluster analysis (HCA) for multivariate association between bioactive compounds and functional properties in foods: a critical perspective, Trends Food Sci. Technol. 72 (2018) 83–90.
[34] J. Auborn, J. Choo, Mechanisms of lubrication in powder metallurgy, Adv. Powder. Metall. Part. Mater. (1993) 17–25.
[35] S. Fernandez, M.I. Nieto, J. Cobos, R. Moreno, CeO_2 pellet fabrication as spent fuel matrix analogue, J. Eur. Ceram. Soc. 36 (2016) 3505–3512.
[36] T. Livneh, E. Sterer, Effect of pressure on the resonant multiphonon Raman scattering in UO_2, Physical Review B 73 (2006) 085118.
[37] H. He, D. Shoesmith, Raman Spectroscopic Studies of Defect Structures and Phase Transition in Hyper-Stoichiometric UO_2+x, Phys. Chem. Chem. Phys. 12 (2010) 8108–8117.
[38] J.M. Elorrieta, L.J. Bonales, N. Rodriguez-Villagra, V.G. Baonza, J. Cobos, A detailed Raman and X-ray study of UO_{2+x} oxides and related structure transitions, PCCP 18 (2016) 28209–28216.
[39] M. Mohammadtaheri, Q. Yang, Y. Li, J. Corona, The Effect of Deposition Parameters on the Structure and Mechanical Properties of Chromium Oxide Coatings Deposited by Reactive Magnetron Sputtering, Coatings 8 (2018) 111 03/19.
[40] A.S.O. Gomes, N. Yaghini, A. Martinelli, E. Ahlberg, A micro-Raman spectroscopic study of $Cr(OH)_3$ and Cr_2O_3 nanoparticles obtained by the hydrothermal method, J. Raman Spectrosc. 48 (2017) 1256–1263.
[41] F. Adar, Raman Spectra of Metal Oxides, Spectroscopy. Solutions for Materials Analysis 29 (2014) 14–24.
[42] S.-.H. Shim, T.S. Duffy, R. Jeanloz, C.-.S. Yoo, V. Iota, Raman spectroscopy and x-ray diffraction of phase transitions in Cr_2O_3 to 61 GPa, Physical Review B 69 (2004) 144107.
[43] Y. Ziouane, B. Arab-Chapelet, S. Lalleman, G. Leturcq, Effect of the Microstructural Morphology on UO_2 Powders, Procedia Chem. 21 (2016) 319–325.
[44] J.M. Elorrieta, L.J. Bonales, M. Naji, D. Manara, V.G. Baonza, J. Cobos, Laser-induced oxidation of UO2: a Raman study, J. Raman Spectrosc. 49 (2018) 878–884.
[45] ASTM E112-13, "Standard Test Methods for Determining Average Grain Size," West Conshohocken, PA, 2013.
[46] K.W. Kang, J.H. Yang, J.H. Kim, Y.W. Rhee, D.J. Kim, K.S. Kim, K.W. Song, Improvement of UO_2 Pellet Properties by Controlling the Powder Morphology of Recycled U_3O_8 Powder, J. Nucl. Sci. Technol. 45 (2008) 1150–1154.
[47] J.H. Yang, K.S. Kim, I.H. Nam, J.S. Oh, D.-.J. Kim, Y.W. Rhee, J.H. Kim, Effect of step wise variation of oxygen potential during the isothermal sintering on the grain growth behavior in Cr_2O_3 doped UO_2 pellets, J. Nucl. Mater. 429 (2012) 25–33.
[48] L. Vegard, Die Konstitution der Mischkristalle und die Raumfüllung der Atome, Zeitschrift für Physik 5 (1921) 17–26.
[49] R. Shannon, Revised effective ionic radii and systematic studies of interatomic distances in halides and chalcogenides, Acta Crystallogr., Sect. A 32 (1976) 751–767.
[50] D.W. Strickler, W.G. Carlson, Ionic Conductivity of Cubic Solid Solutions in the System CaO—Y_2O_3—ZrO_2, J. Am. Ceram. Soc. 47 (1964) 122–127.
[51] Y. Harada, Sintering behaviour of niobia-doped large grain UO_2 pellet, J. Nucl. Mater. 238 (1996) 237–243.
[52] P.G. Marlow, J.P. Russell, J.R. Hardy, Raman scattering in uranium dioxide, The Philosophical Magazine: A Journal of Theoretical Experimental and Applied Physics 14 (1966) 409–410.
[53] J.J. Arnoux, G. Sutter, G. List, P. Bourson, H. Chaynes, Raman characterization of Ti–6Al–4 V oxides and thermal history after kinetic friction, Phase Transitions 87 (2014) 559–570.
[54] M.-.F. Luo, P. Fang, M. He, Y.-.L. Xie, In situ XRD, Raman, and TPR studies of CuO/Al_2O_3 catalysts for CO oxidation, J. Mol. Catal. A Chem. 239 (2005) 243–248.
[55] S.E. Molis, D.R. Clarke, Measurement of Stresses Using Fluorescence in an Optical Microprobe: stresses around Indentations in a Chromium-Doped Sapphire, J. Am. Ceram. Soc. 73 (1990) 3189–3194.

[56] D. Manara, B. Renker, Raman spectra of stoichiometric and hyperstoichiometric uranium dioxide, J. Nucl. Mater. 321 (2003) 233–237.
[57] R. Rao, R.K. Bhagat, N.P. Salke, A. Kumar, Raman Spectroscopic Investigation of Thorium Dioxide–Uranium Dioxide (ThO_2–UO_2) Fuel Materials, Appl Spectrosc 68 (2014) 44–48.
[58] L. Desgranges, G. Baldinozzi, P. Simon, G. Guimbretière, A. Canizares, Raman spectrum of U_4O_9: a new interpretation of damage lines in UO_2, J. Raman Spectrosc. 43 (2012) 455–458.